Supported-Single Nickel Atom Catalysts for the Methanation of Carbon Dioxide

Carly Byron,[a] Yu Lim Kim,[a] Jacob T. Bryant,[a] Jacklyn N. Hall,[a] Tao Zhou,[b] Jianguo Wen,[b,*] Cong Liu,[a] Massimiliano Delferro[a,*] and Magali S. Ferrandon[a,*]

[a] Chemical Sciences and Engineering Division, Argonne National Laboratory, Lemont, IL, USA 60439

[b] Center for Nanoscale Materials, Argonne National Laboratory, Lemont, IL, USA 60439

Emails: jwen@anl.gov; delferro@anl.gov; ferrandon@anl.gov

KEYWORDS: Single atom • methanation • CO_2 conversion • nickel • promoter • high-throughput screening

ABSTRACT: Synthesis of twenty-seven bimetallic catalysts consisting of nickel and one of nine different dopants (B, Co, Cu, Fe, Mg, Mn, Sn, V and Zn) supported on three different metal oxides (Al_2O_3, CeO_2, and SiO_2) is carried out via organometallic grafting. The catalysts are evaluated for their activity and selectivity for the CO_2 methanation reaction at a feed ratio of H_2:CO_2 of 4 at 300 °C in a high-throughput flow reactor system. After *in-situ* pre-activation (500 °C in H_2), Ni/Co/CeO_2 exhibited high conversion (84.3 %) and selectivity for methane (99.6 %). Ni/Co/CeO_2 was characterized by High-Resolution Transmission Electron Microscopy (HRTEM), X-Ray Photoelectron Spectroscopy (XPS), X-Ray Diffraction (XRD), H_2-Temperature-Programmed Reduction (H_2-TPR), and CO_2-Temperature-Programmed Desorption (CO_2-TPD). HRTEM showed the presence of single Ni and Co atoms on ceria after pre-reduction at 500 °C and after the methanation reaction at 300 °C for 15 h. XPS determined that the strong interaction between Ni, Co, and ceria increased after the reduction, leading to a charge transfer between Ni and Ce which created oxygen vacancies in ceria. Nickel was found to be Ni^{2+} in the as-prepared material and was partially reduced in the presence of cobalt and after the activation in H_2 at 500 °C. The DFT results show that both nickel and cerium exhibit lower Bader charges in the Ni/Co/CeO_2 system, confirming that the presence of cobalt enhances the reduction of both Ni and Ce through electronic interactions. This indicates that single cationic Ni atoms are highly effective for the methanation reaction. The organometallic grafting technique is found to be efficient for synthesizing catalyst with highly and homogeneous dispersed species at low metal loadings (0.16 wt.% Ni – 0.15 wt.% Co) which lead to high turnover frequency (up to 248.7 h^{-1}) and durability for methanation.

Introduction

Methane is a main component in natural gas and shale gas. Substitute or synthetic natural gas (SNG) was proposed during the start of the energy crisis in the 1970s. Today, SNG is becoming important as its production may potentially enhance the diversity of energy and chemical feedstocks. The infrastructure for its delivery is well developed and equipped throughout the world. This makes SNG an excellent energy carrier.[1] SNG has been commercially produced from different starting materials including coal and biomass. In this process, syn-gas (CO and H_2) is transformed into methane (Eq. 1):

$$CO + 3H_2 \leftrightarrow CH_4 + H_2O \;\; \Delta^o H_{298K} = -206\ kJ\ mol^{-1} \quad (1)$$

CO_2 is an abundant C1 feedstock that is widely studied for utilization and conversion into valuable chemicals. The conversion of CO_2 to methane with H_2, also called Sabatier reaction (Eq. 2), has gained great attention because of its usage in the power-to-gas technology.[2]

$$CO_2 + 4H_2 \leftrightarrow CH_4 + 2H_2O \;\; \Delta^o H_{298K} = -165\ kJ\ mol^{-1} \quad (2)$$

From a thermodynamic point of view, CO_2 methanation is exothermic and releases a large amount of heat.[3]

Precious metals such as Ir, Ru, Pd and Rh have been reported to be active for methanation of CO_2.[3–8] However, the high cost and low availability of these noble metals are considered the main drawbacks that inhibit their use on an industrial scale.[4] Ni catalysts have high activity and CH_4 selectivity, but suffer from particle sintering, due to the exothermicity of the reaction, and coke formation.[1,3,4,9,10] To circumnavigate this problem, bimetallic systems, in which a promoter metal is added, have been used to improve Ni activity and selectivity.[9] In particular, transition metals (e.g. Fe, Co, Cu and Mn) have been shown to improve Ni activity,[11,12] as well as non-transition metal additives (e.g. B, Mg, La).[13–15]

The choice of the support also plays an important role by providing anchoring sites, high surface area, increased oxygen storage capacity, higher basicity or acidity, increased thermal stability, and resistance to carbon deposition and deactivation. Typical supports for Ni-catalyzed methanation of CO_2 are Al_2O_3,[9,16] SiO_2,[16] TiO_2,[16,17] ZrO_2,[11,16] and CeO_2.[16,18–20] CeO_2 tends to sinter at high temperatures[21] and even to a high extent at high loadings of metals.[22] Note also that the methanation performance is sensitive to particle size of Ni;[23] undercoordinated Ni sites and subnanometer Ni have been reported to be highly selective for CO_2 methanation.[24,25] In addition, isolated Ni atoms are more resistant to carbon deposition due to their ability to activate the C-H bond of CH_4 and avoid decomposition into atomic carbon.[23] Note also that most literature reports very high loadings of active metals in the range of 10 to 20 wt.% [1,9,11,15,19,24,26] and, to the best of our knowledge, none have reported on isolated single-atom Ni sites for the methanation of CO_2.

Standard techniques for synthesizing methanation catalysts such as incipient wetness impregnation (IWI) often lead to formation of large particles or agglomerates.[10] More advanced

syntheses techniques have been reported, such as sol-gel,[19] evaporation impregnation method,[25] chelation coupled impregnation,[20] and soft and hard templates for support-free catalysts.[27] Overall these techniques contain a broad distribution of metal coordination environments while only a small portion participates in catalysis.[28] Surface organometallic chemistry (SOMC), which utilizes organometallic compounds to graft metal atoms onto oxide supports at surface concentrations of less than a monolayer coverage, has been shown to produce isolated metal atoms or highly-dispersed nanoparticles (< 1nm) with a narrow particle size distribution depending on the heat treatment.[29] These highly dispersed metal nanoparticles tend to minimize surface energy by increasing interaction with the support which helps stabilize the particles from sintering.[30] The main advantage of SOMC lies in its ability to generate surface sites with well-defined active sites, thus facilitating structure–activity relationship studies.

Previously, the screening of catalyst synthesized via SOMC using combinatorial platforms allowed the accelerated discovery of new catalyst compositions.[31–34] The catalytic performance of Ni-based catalysts, in terms of activity, selectivity, and stability, could be enhanced by depositing a submonolayer of promoters with the aim of increasing nickel dispersion, reducibility, and interaction with the modified support. Specifically, this work reports the systematic synthesis of 27 different combinations of Ni and additives such as B, Cu, Co, Fe, Mn, Sn, Mg, V, and Zn onto oxide-supports including Al_2O_3, CeO_2, and SiO_2 by first grafting the promoter using organometallic precursors followed by calcination, and finally depositing the Ni using bis(N,N'-di-t-butylacetamidinato)nickel (II) as metal precursor (Scheme 1). These additives were chosen because they are in the first row of transition metals such as V,[35] Mn,[11,36,37] Fe,[11,12] Co,[11,38] Cu,[11], Zn,[39], and Mg.[14] B was chosen for its coke prevention.[40] These catalysts were then screened using a parallel flow reactor for the methanation reaction at temperatures ranging from 200-300 °C to identify any combination(s) of promoter and support that lead to an improvement in reactivity and stability over the non-promoted nickel catalysts for the production of methane.

Experimental Section

Materials. Commercially available γ-Al_2O_3 (STREM Chemicals, > 97 %), CeO_2 (nanopowder < 50 nm, 99.95 %, Aldrich), and SiO_2 (Selecto, 30-200 μm size, pore size *ca.* 6 nm, surface area 520 m^2/g) were used. All supports were vacuum dried at 200 °C overnight. Some organometallic precursors were purchased: triisopropyl borate (> 98 % Sigma-Aldrich), bis(N-t-butyl-N'-ethylpropanimidamidato)cobalt (II) (> 98 % STREM Chemicals), bis(dimethylamino-2-propoxy)copper (II) (STREM Chemicals, > 97 %), 2,2-dimethylpropylmagnesium chloride solution (1 M in THF, Sigma-Aldrich), bis(N,N'-di-t-butylacetamidinato)nickel (II) (STREM Chemicals, 99.999 %), tetramethyltin (STREM Chemicals, 98 %), diethylzinc (II) (Sigma-Aldrich), bis(N,N'-di-i-propylpentylamidinato)manganese (II) (STREM Chemicals, 98 %). The $[V(Mes)_3(THF)]$ complex was prepared as reported in the literature.[41] The $[Fe(\mu\text{-}Mes)Mes]_2$ complex was prepared according to a modified literature procedure[42] where the mixture was left to react overnight and the dioxane added 2 h before workup. Anhydrous toluene (Aldrich) was purged with N_2, and further dried over activated alumina for 24 h, and tested for dryness with sodium benzophenone ketyl before use. All gases were purchased from Airgas and were UHP grade.

Combinatorial Catalysis Synthesis. An automated synthesis platform (CM3 Core Module deck, Unchained Labs Inc.) housed in a custom-built N_2-filled glovebox (MB 200B, MBraun) was used for the catalyst syntheses. A two-step surface organometallic chemistry process was used for depositing first the promoters followed by the deposition of Ni onto each of the supports (Scheme 1). The amount of organometallic precursor was calculated based on the desired coverage (50% of a monolayer). The monolayer was calculated based on the surface area and the OH sites density, which were determined by the BET and thermogravimetric analyses, respectively (Table S1). For each combination, 600 mg support was weighed in an 8 mL glass vial pre-loaded with a magnetic stir bar. Under stirring, the solid supports were pre-wetted with dry toluene to ensure homogeneous deposition of metal precursors. Various stock solutions of precursors in toluene were then dispensed into each vial. After dispensing the stock solution, additional toluene was dispensed to adjust the total liquid volume to 4 mL. The 24 well plates of vials were then placed manually onto a shaker plate and let shake for 24 h at 400 rpm at room temperature. The well plates were then centrifuged (Speedvac Concentrator, Savant SPD121P, ThermoElectron), two well plates at a time, for 10 min and then the supernatant was removed, and 2 mL fresh toluene was added. The procedure was repeated 5 times. After removal of the last supernatant, the vials were then removed from the glovebox and placed under air environment to dry. The samples were then calcined in air at 450 °C for 2 h. The solids were then brought back into the glovebox for the addition of nickel precursor. The same procedure was repeated as above. Samples were labeled Ni/promoter/support. Two additional catalysts were synthesized. The first one, Ni-Co was synthesized without any calcination after deposition of Co, only with a drying step carried out inside the glovebox before the deposition of Ni. The second one (Co/Ni) is similar to Ni/Co but with Ni deposited first, calcined at 450 °C, followed by deposition of

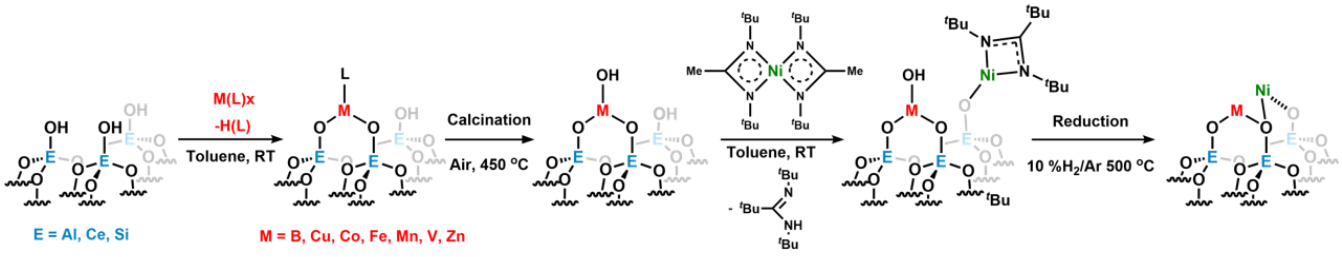

Scheme 1. Schematic of the multi-step surface organometallic chemistry (SOMC) process for synthesizing bimetallic catalysts: (1) deposition of organometallic promoter sites onto an oxide support followed by calcination at 450 °C; (2) deposition of organonickel onto modified oxide support; and (3) *in-situ* reduction.

cobalt. All the samples were stored outside the glovebox and tested as-is. Elemental analyses are indicated in Table 1 for all samples.

Table 1. List of samples and the elemental analyses (wt.%) of Ni and promoter.

	Al_2O_3	CeO_2	SiO_2
Ni	4.21	0.611	4.128
Ni/B	2.83/0.38	0.98/0.15	1.03/0.15
Ni/Co	3.25/3.11	0.16/0.15	0.39/0.59
Ni/Cu	3.17/2.76	1.61/0.80	0.43/0.74
Ni/Fe	3.95/5.14	0.77/1.06	4.10/1.08
Ni/Mg	4.26/0.29	0.65/1.27	4.02/0.11
Ni/Mn	3.11/3.16	0.89/0.54	0.40/0.59
Ni/Sn	3.11/0.06	2.31/n.d.	0.46/<lod [a]
Ni/V	3.65/1.52	1.22/0.10	0.39/0.40
Ni/Zn	3.0/1.70	1.28/0.10	0.42/0.10
Co/Ni	-	0.89/0.61	-
Ni-Co	-	0.46-0.37	-

[a] limit of detection

High-Throughput Catalysis Screening. A 16-channel high-throughput fixed bed system (Flowrence® from Avantium) was used for the catalytic experiments. 50 mg catalyst was mixed with 50 mg Silica Davisil (Sigma-Aldrich 230 mesh) and loaded into a quartz reactor (2 mm ID, 30 mm length). Blank and support oxides were also tested for comparison and had negligible conversion. The error on the measurement was estimated to be less than 2 % when using the exact same conditions. Total flow rates for each reactor of either 6 or 9 mL/min were used, of which 3 mL/min H_2, 1 mL/min He and varying flowrates of 30 % CO_2/Ar and N_2 to keep the total flowrate the same (Table S2). This gives a H_2:CO_2 = 5.4, 4.0, 3.0 and 2.0. The weight hourly space velocity was 11,000 h^{-1} at 9 mL/min total flowrate. He was used as a GC internal standard. The catalysts were pre-activated *in-situ* at 500 °C in 10% H_2/Ar for 2 h or in N_2 to determine the effect of pre-reduction. The temperatures tested were 200 to 300 °C (5 °C/min) with an increment of 50 °C, followed by a stability testing at 500 °C for 15 h. Carbon balance was over 95 %. At each temperature, a gas sample was taken automatically, sequentially from reactor #1 to reactor #16, for gas chromatography (7890B, Agilent Technologies). Each gas sample was flushed for 11 min before the analysis. The effluent of each reactor was analyzed sequentially by a gas chromatograph, equipped with a thermal conductivity detector (TCD) and two flame ionization detectors (FID) and 4 columns: HP-AL/S (25m x 0.320mm) and DB-FFAP (30 m x 0.320 mm) (Agilent Technologies), molecular sieve 5A 80/100 6' 1/8" and Hayesep Q 80/100 6' 1/8" (Restek). The main products, besides methane, were carbon monoxide, and ethane. Carbon balance was between 98 and 100 %. The conversion of CO_2 was calculated based on the concentration of CO_2 in the inlet and outlet of gas flow using He as internal standard using Eqn. 3:

$$CO_2\ conversion\ (\%) = \frac{([CO_2\ in] - [CO_2\ out]) \times 100}{[CO_2\ in]} \quad (3)$$

The selectivity of each carbon-containing product was calculated by Eqns. 4-6:

$$CH_4\ selectivity\ (\%) = \frac{[CH_4\ out] \times 100}{[C_2H_6\ out] \times 2 + [CH_4\ out] + [CO\ out] + [CO_2\ out]} \quad (4)$$

$$CO\ selectivity\ (\%) = \frac{[CO\ out] \times 100}{[C_2H_6\ out] \times 2 + [CH_4\ out] + [CO\ out] + [CO_2\ out]} \quad (5)$$

$$C_2H_6\ selectivity\ (\%) = \frac{[C_2H_6\ out] \times 100}{[C_2H_6\ out] \times 2 + [CH_4\ out] + [CO\ out] + [CO_2\ out]} \quad (6)$$

Characterization. *Transmission electron microscopy* (TEM) was used to probe for the presence of single atom, nanoparticles or clusters; however, it should be noted that sample preparation for TEM analyses (sonication in ethanol) as well as imaging conditions (a 200 kV electron beam) could change material composition *in-situ* (e.g., metal agglomeration). Samples were prepared by dispersing solids in ethanol via sonication for 30 s. Colloidal suspensions were drop cast onto TEM grids. A scanning transmission electron microscope, a FEI Talos F200X TEM/STEM operated at 200kV, was used for energy-dispersive X-ray spectroscopy (EDS). Particle size and shape were measured using ImageJ[43] and Gatan Digital Micrograph software. Aberration-corrected high angle annular dark-field (HAADF) imaging, electron energy loss spectroscopy (EELS) and cathodoluminescence (CL) spectroscopies were acquired using the Quantum Emitter Electron Nanomaterial Microscope (QuEEN-M), a Spectra 300 STEM with an Attolight CL system, located in the Center for Nanoscale Materials (CNM) at Argonne National Laboratory.

Surface area of the catalyst was measured by the Brunauer–Emmett–Teller (BET) method at liquid nitrogen temperature using a Micromeritics ASAP2020 surface area analyser. The samples were first evacuated under dynamic vacuum (< 10^{-3} torr) at 130 °C overnight to remove the guest molecules and adsorbed moisture before re-measuring the accurate sample weight.

Elemental analysis was performed at QBIC (Northwestern University, Chicago) using a Thermo iCap7600 ICP-OES instrument. Approximately 30 mg of sample was digested in 1 mL of HF and subsequently diluted to 11 mL with a 0.9 wt.% HNO_3 aqueous solution. Standards of known concentration were prepared to quantify the samples' metal content.

Thermogravimetric Analysis (TGA) was carried out using a Discovery (TA Instruments) coupled with a mass spectrometer (QMS200, Stanford Research Systems) with 10 mL/min N_2.

H_2-temperature-programmed reduction (H_2-TPR) studies were carried out in an Altamira (AMI-100) system. A mixture of 3 % H_2/N_2 at atmospheric pressure was used. Samples of 40 mg were loaded into a quartz U-tube reactor. The H_2-TPR profiles were obtained by flowing H_2/Ar mixture at 50 mL/min from 30 to 700 °C at 10 °C/min. The hydrogen consumption was monitored quantitatively using a thermal conductivity detector.

The crystalline phase compositions of H_2-TPR reduced catalysts (up to 700 °C) were determined by *powder X-ray diffraction* (PXRD) using a Bruker Diffractometer D8 Advance operating with the following parameters: Cu Kα radiation of 40 mA, 40 kV, K_λ = 0.15418 nm, 2θ scanning range of 10-70°, a scan step size of 0.0018º and a time of 1s per step. The sample was ground and placed on a zero-background silicon holder (MTI Corp.) for analysis.

The *CO_2-temperature-programmed desorption (CO_2-TPD)* analyses were carried out in Autochem 2920 (Micromeritics). 50 mg of samples were first reduced at 500 °C for 4 h with 50 mL/min 10 % H_2/Ar, then cooled down to room temperature, flushed with He for 1 h at 50 mL/min. Ten pulses of CO_2 were applied at room temperature, followed by desorption in 50 mL/min He up to 800 °C.

X-ray photoelectron spectroscopy (XPS) was performed using a K-Alpha+ XPS system (Thermo Scientific) using an Al K-Alpha X-ray source (hv=1486.6 eV), with a takeoff angle of 35.3° with respect to the analyzer. The "as-is" and "spent" samples were exposed to air before analysis. Two "reduced" samples, Ni/Co and Co/Ni, were reduced at 500 °C in 10 % H_2/Ar and brought to the N_2-glovebox to load the samples in the vacuum transfer module (ThermoFisher Scientific) before bringing them into the XPS instrument for ensuring no reoxidation of the samples. The high-resolution spectra were collected with a pass energy of 60 eV, and the survey spectra were collected over the 0-1000 eV binding energy range. CasaXPS software was used to analyze and calibrate the raw data. The XPS scale was calibrated to the carbon 1s C-C peak at 284.6 eV.[44,45]

Computational methods for density functional theory calculations can be found in the Supporting Information.

Results and Discussion

Reaction Conditions Optimization. Ni/promoter/CeO_2 catalysts were selected to study the effects of temperature, H_2/CO_2 ratios (5.4; 4.0, 3.0 and 2.0; Figure S1a and S1b) and flow rate (Figure S2). Note also that variation in pressure was not evaluated, as it is understood that methanation performs more effectively at low pressure.[46] As expected, an increase in temperature increases the conversion, as shown by the calculated equilibrium conversion (Figure S3a).

The effect of H_2/CO_2 ratio was investigated on Ni/promoter/CeO_2 catalysts, as seen in Figure S1b. An increase in H_2 concentration increases the conversion of CO_2 due to increased equilibrium conversion (Figure S3b). Note the absence of carbon at H_2/CO_2 = 4.0 (Figure S3a). In order to avoid coke formation, indeed a minimum ratio of 4.0 is usually recommended as it provides enough water to suppress C.[46] Thermodynamically calculated CO_2 conversion values at 300 °C are as follows: 99.9 % for H_2/CO_2 = 5.4 and 92.1 % for H_2/CO_2 = 4. Most literature reports CH_4 production from CO_2 at 270 - 400 °C.[4] A lower temperature is preferred because of the higher CH_4 selectivity due to the less endothermic reverse water gas shift reaction (Eq. 7) producing CO at higher temperature.

$$CO_2 + H_2 \leftrightarrow CO + H_2O \quad \Delta^o H_{298K} = 41.2\ kJ\ mol^{-1} \qquad (7)$$

Catalyst Screening. Therefore, a temperature of 300 °C was selected with a H_2/CO_2 ratio of 4 for the catalyst screening. The CO_2 conversion at 300 °C and H_2/CO_2 = 4 of Ni, Ni/B, Ni/Co, Ni/Cu, Ni/Fe, Ni/Mg, Ni/Mn, Ni/Sn, Ni/V and Ni/Zn catalysts are shown in Figure 1a, while methane selectivities are shown in Figures 1b, 1c and 1d, for Al_2O_3, CeO_2 and SiO_2, respectively. The CO_2 conversion is relatively low and similar for monometallic Ni on all supports (40, 32 and 41 % for

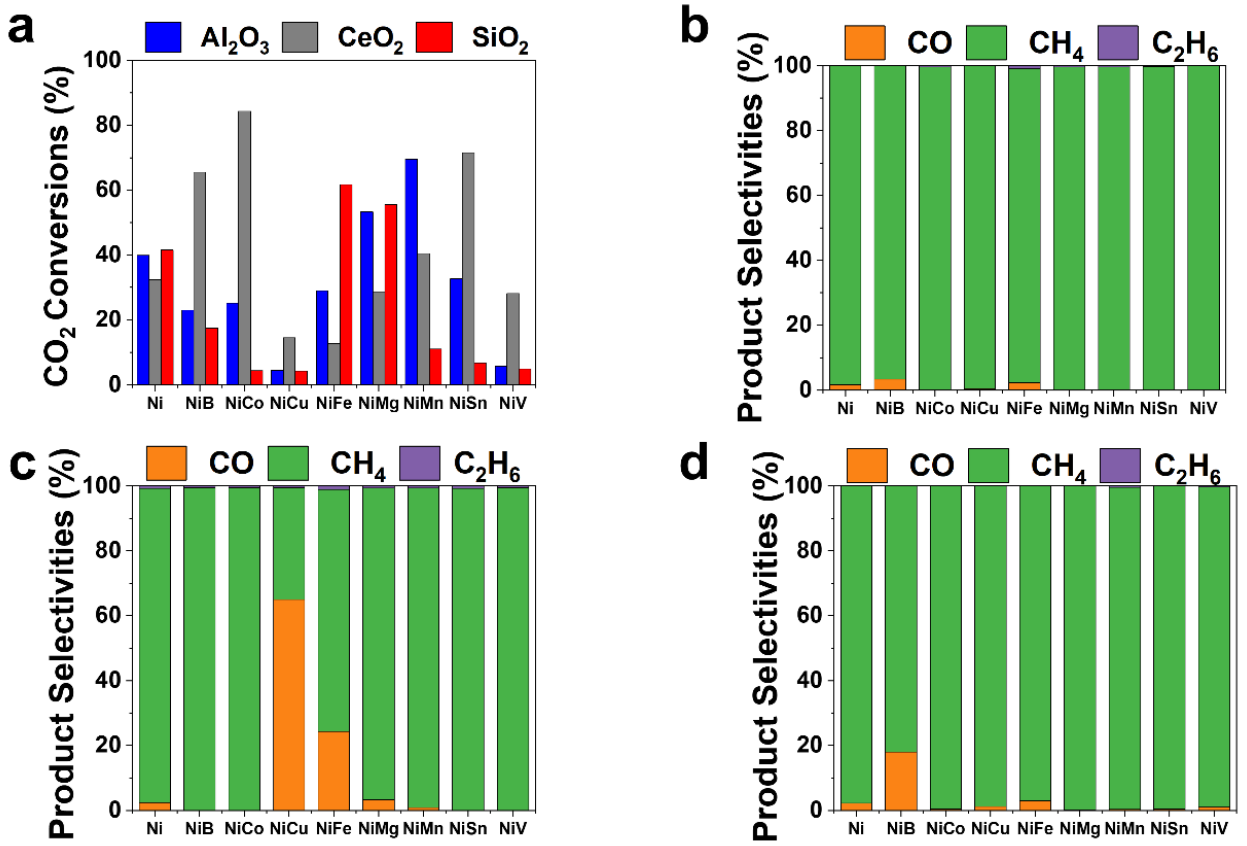

Figure 1. a) CO_2 conversion for all Ni-based catalysts; b) CO, methane and ethane selectivities for Ni/promoter/Al_2O_3; c) Ni/promoter/CeO_2; d) and Ni/promoter/SiO_2. Conditions: H_2/CO_2 = 4, 300 °C. Pre-reduction in 10 % H_2/Ar for 2 h at 500 °C.

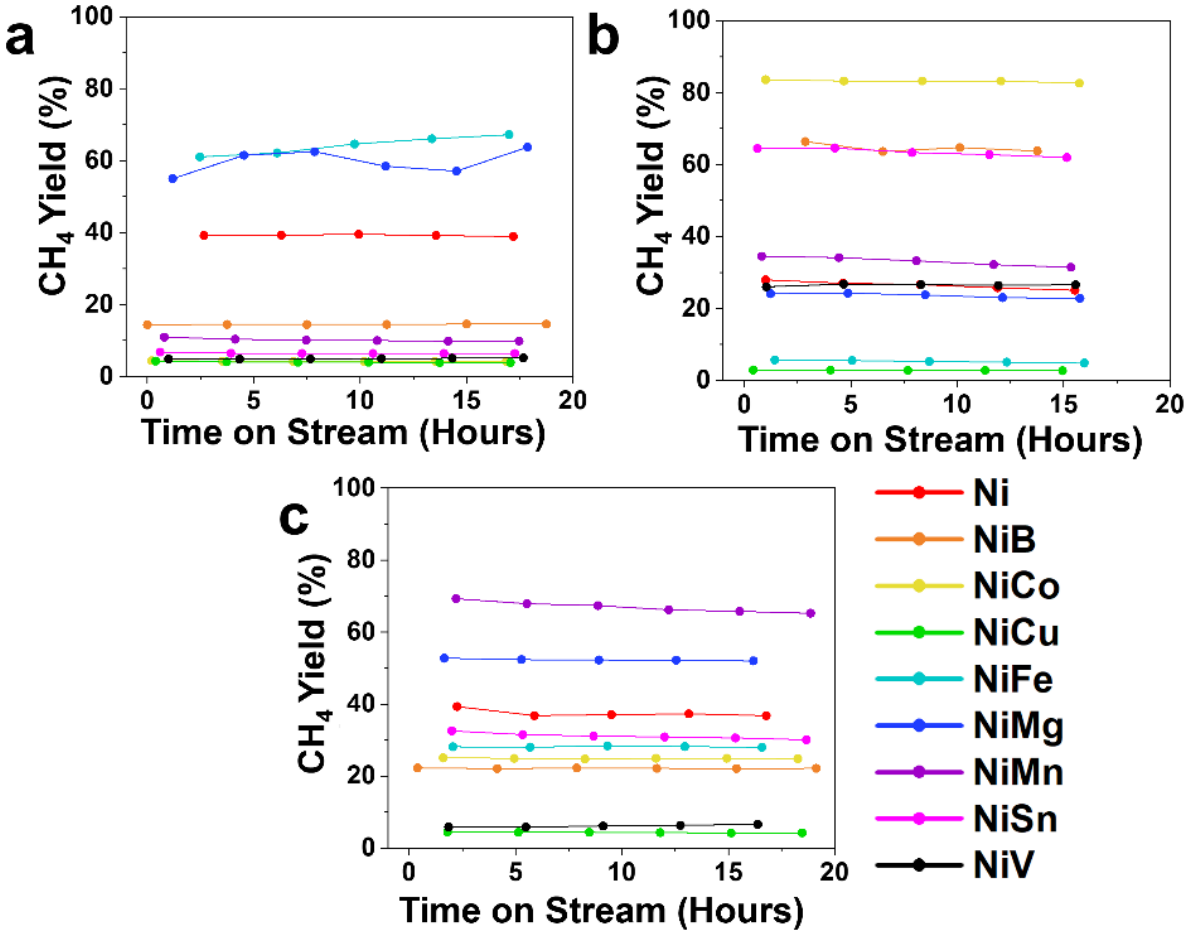

Figure 2. Methane yield for the catalysts supported on Al_2O_3 (a), CeO_2 (b) and SiO_2 (c). Conditions: 300 °C, H_2/CO_2 = 4. Pre-reduction in 10 % H_2/Ar for 2 h at 500 °C.

Ni/Al_2O_3, Ni/CeO_2 and Ni/SiO_2, respectively). However, the presence of promoters affects the conversion significantly, both positively and negatively. For Ni/promoter/Al_2O_3, only Mg and Mn improved the conversion of CO_2 over that of Ni alone while for Ni/promoter/CeO_2, only B, Co, Mn and Sn, and for Ni/SiO_2, only Mg enhanced the conversion of CO_2 over that of Ni alone. The selectivity to methane is above 99 % for Ni/Co, Ni/Cu, Ni/Mg, Ni/Mn Ni/Sn and Ni/V on Al_2O_3, for Ni/B, Ni/Co, Ni/Sn and Ni/V on CeO_2 and Ni/Co, Ni/Mg, Ni/Mn, Ni/Sn on SiO_2. In this study, Ni/Zn/CeO_2 has high selectivity to CO. A small fraction of ethane is also observed due to the hydrogenation of ethylene formed by deoxygenative coupling of CO (<1%). No alcohol (e.g methanol or ethanol) or other functionalized products (e.g. formaldehyde, formic acid) were observed under the current reaction conditions.

In this study, the highest CO_2 conversions at 300 °C are obtained for Ni/Co/CeO_2, 84.3 % at H_2/CO_2 = 4.0, which is close to the calculated equilibrium conversion (Figure S3b). Compared to other reported catalysts under similar reaction conditions (Table 2), Ni/Co/CeO_2 exhibits excellent performance.[9,18–20,25,26,38,47–50]

Stability evaluation of Ni-promoter. Short-term testing was performed on all catalysts for over 15 h on-stream, which is shown in Figure 2a-c. On-stream gas evaluation shows that nearly all the catalysts were relatively stable, with very little performance drop over time. The highest methane yields were observed on CeO_2-supported catalysts, leading with Ni/Co/CeO_2 (84.0 %), followed by Ni/B/CeO_2 (66.4 %), and Ni/Sn/CeO_2 (64.5 %). On Al_2O_3, the highest methane yield was observed with Ni/Mn (69.3%), and on SiO_2, the highest yields from Ni/Fe and Ni/Mg increased slightly over time (61 → 67.2% and 55 → 63.7%, respectively). Note also that the superiority of CeO_2 over other supports on stabilizing single atoms catalyst is in agreement with previously reported work.[21] The beneficial impact of the promoter was unmistakable; Ni alone had yields lower than 40 % after 15 h

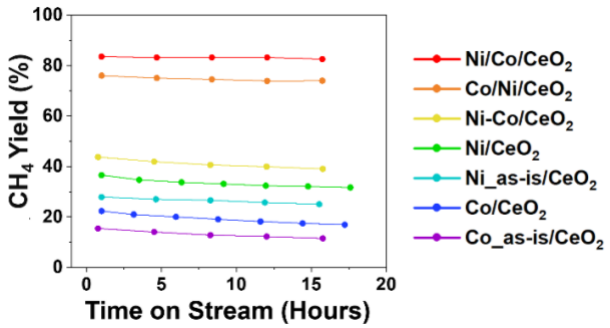

Figure 3. Methane yields for Co_as-is/CeO_2, Co/CeO_2 (calcined at 450 °C), Ni/Co/CeO_2 (Ni deposited on calcined Co/CeO_2), Ni_as-is/CeO_2, Ni/CeO_2 (calcined at 450 °C), Co/Ni/CeO_2 (Co deposited on calcined Ni/CeO_2) and Ni-Co/CeO_2 (Co deposited then Ni, drying step in between). Conditions: H_2/CO_2 = 4, 300 °C. Pre-reduction in 10 % H_2/Ar for 2 h at 500 °C.

Table 2. Comparison with other Ni- and Co-based catalysts.

Catalyst	Ratio	Temp (°C)	GHSV (mL/g/h)	CO_2 Conv. (%)	CH_4 Sel. (%)	References
5% Ni/CeO_2-Cub	1:4	275	800	59.6	100	18
10%Ni/CeO_2	1:4	275	24,000	84.3	100	20
0.16%Ni/0.15%Co/CeO_2	1:4	300	11,000	84.3	99.6	This work
5%Ni2.5%Ce13X	1:4	320	13,333	80	100	25
20% Ni/Al_2O_3	1:4	325	120,000	90	100	9
18% Ni/CeO_2	1:4	350	8,000	60	100	19
30Ni/Al_2O_3-0.5SiO_2	1:3.5	350	9,000	82.4	98.2	47
15%Ni/C-CeO_2	1:4	370	60,000	87.4	100	26
Ni_3Co_2-C	1:4	380	60,000	64	95	26
NiCo-HT	1:4	380	60,000	68	98	48
8%Ni2%Co/Al_2O_3	1:4	400	15,000	80	97.5	38
1.3%Ni/CeO_2	1:4	400	12,000	70	98	49
10%Ni3%Co/Al_2O_3	1:4	400	10,000	78	99	50
5% Ni/CeO_2-Cub	1:4	275	800	59.6	100	18

across all supports. Due to the large amount of information obtained from catalyst screening, only the most active bimetallic pairings (Ni and Co on CeO_2) were investigated further in the present study.

Effect of deposition order on the activity and stability. In order to evaluate any synergistic effects between Ni and Co and whether the deposition of metals order affects the activity, the yields for over 15 h for the individual metals are compared in Figure 3 for Ni/CeO_2, Co/CeO_2, Ni/Co/CeO_2 (Ni deposited on Co/CeO_2 after calcination), Co/Ni/CeO_2 (Co deposited on Ni/CeO_2 after calcination) and Ni-Co/CeO_2 (Ni deposited on Co on CeO_2 after drying).

In addition, the turnover frequency (TOF) and deactivation constant (k_d) are presented in Table 3. Yields for both single components (27.9 % for Ni and 15.4 % for Co) are significantly lower than that for Ni/Co, Co/Ni and Ni-Co. The

Table 3. Turnover frequency (TOF) and deactivation rate calculated based on CO_2 conversion at 300 °C.

Catalyst	TOF (h^{-1})	k_d[a] (h^{-1})
Ni_as-is/CeO_2	39.5	0.0099
Co_as-is/CeO_2	91.4	0.0225
Ni/CeO_2	51.8	0.0131
Co/CeO_2	129.5	0.0220
Ni/Co/CeO_2	248.7	0.0048
Co/Ni/CeO_2	43.8	0.0072
Ni-Co/CeO_2	45.7	0.0132

[a] Deactivation constant, $k_d = \frac{ln\left(\frac{1-Yf}{Yf}\right) - ln\left(\frac{1-Yi}{Yi}\right)}{Tf - Ti}$

TOF, which was calculated based on the total amount of metal, shows a significant increase when Ni was deposited on Co compared to Ni alone on CeO_2. The large TOF for Ni/Co (248.7 h^{-1}) compared to Ni (51.8 h^{-1}) was not only due to the high yield but also the very low loadings of nickel (0.158 wt.%) and cobalt (0.146 wt.%) compared to Ni alone (0.611 wt.%). Ni/Co/CeO_2 shows some very slight deactivation over 15 h (k_d = 0.0048 h^{-1}); however, to a lesser extent compared to monometallic Co and Ni (0.0099 h^{-1} for Ni and 0.0225 h^{-1} for Co). Ni-Co gave a lower yield (43 %), and a higher deactivation rate compared to Ni/Co. Co/Ni/CeO_2 gave the second-best methane yield (76 %) after Ni/Co/CeO_2. second-best methane yield (76 %) after Ni/Co/CeO_2. The highly active Ni/Co/CeO_2 was also tested for a longer time of 60 hours to investigate catalyst stability, shown in Figure S4. The methane yield remained above 80% and exhibited minimal deactivation.

For catalysts compared with and without the calcination step (Ni/CeO_2 and Co/CeO_2), the calcined catalyst performed consistently better than the as-is catalyst. In addition to the effect of deposition order, the effect of pre-activation in H_2 was studied. When Ni/Co was not reduced *in-situ* it shows a lower methane yield (44 %) compared to *in-situ* reduction at 500 °C (Figure S5). If the catalyst is pre-reduced at 500 °C and re-exposed to air at ambient conditions, the yield improves slightly (63 %) compared to no reduction.

Characterization of Ni- and Co-based catalysts. In order to evaluate the temperature at which the organic residues from the bis(N,N'-di-t-butylacetamidinato)nickel precursor decompose and whether traces were still present on the as-prepared sample, thermogravimetric analysis (TGA) of the as prepared Ni/Co/CeO_2 (Ni deposited on calcined Co/CeO_2) was measured (Figure S6). This was compared with the TGA of calcined Co/CeO_2, showing negligible changes in weight above 200 °C and no CO_2 evolution. For the as prepared Ni/Co/CeO_2, the CO_2 peak below 320 °C corresponds to the decomposition of the organic residues from the nickel precursors. The weight loss calculated between 200 and 320 °C corresponds to the fraction of precursors (without Ni) based on the weight percentages from ICP of the material, indicating that the calcination step was essential in removing the precursor organic ligands.

The XRD spectra of CeO_2, Ni/CeO_2, Co/CeO_2, Ni/Co/CeO_2 Co/Ni/CeO_2 and Ni-Co/CeO_2 after reduction (Figure S7) does not show the presence of Ni^0 peaks (2θ = 44.5°, 51.8° PDF 00-001-1258) nor NiO peaks (2θ = 37.2°, 43.2°, 62.8° PDF 01-073-1523) or Co species, indicating that Ni and Co are highly dispersed and/or the concentrations of Ni and Co species are below the detection limit of XRD.

High-resolution transmission electron microscopy was employed to analyze the distribution of single atoms. Figure 4a presents an atomic-resolution high-angle annular dark-field (HAADF) image of representative CeO_2 nanoparticles. The image was acquired with a cutoff angle exceeding 75 mrad, ensuring Z-contrast imaging where intensity scales with

Z^n ($n \approx 2$). The brighter dots are Ce atoms while the dimmer dots are either Ni and Co atoms with low atomic numbers or Ce vacancies.

Scanning transmission electron microscopy-electron energy loss spectroscopy (STEM-EELS) was applied to map these single atoms which have lower Z than that of the matrix. Figure 4b illustrates a STEM-EELS map, identifying observed Co and Ni single atoms within the CeO_2 nanoparticles. Figures 4c–4e display the EELS spectra for CeO_2 nanoparticles and single Co and Ni atoms. Due to the trace amounts of Co and Ni, no distinct signals corresponding to the Co $L_{2,3}$ and Ni $L_{2,3}$ edges are observed in the CeO_2 EELS spectrum integrated from the whole area (Figure 4c). Only the summed EELS from single Co or Ni atoms show distinguishable $L_{2,3}$-edges compared to areas without Co and Ni atoms (Figures 4d–4e).

From the STEM-EELS mapping (Figure 4b), no aggregation of Co or Ni is observed. Additionally, no significant concentration at the surface of CeO_2 nanoparticles is detected, indicating that Co and Ni atoms are incorporated within the CeO_2 lattice. Figures 4g–4h display cathodoluminescence (CL) microscopy of CeO_2 nanoparticles doped with single Co and Ni atoms. In the CL spectrum, the broad peak around 650 nm is attributed to CeO_2, with its width and position influenced by oxygen vacancies and Fe impurities in CeO_2.[51] CL spectroscopy revealed two distinct emission peaks at approximately 880 nm and 900 nm,[52] corresponding to electronic transitions within the d-orbitals of Co ions ($^4T_1 \rightarrow {}^4A_2$). These peaks are associated with the oxidation state of Co^{2+} and its specific coordination environment within the CeO_2 matrix. After reaction for 15 h at 300 °C, no agglomeration was observed by HAADF (Figures S8 and S9) indicating that the Ni and Co are stabilized onto CeO_2. Ni and Co adsorption on CeO_2 caused significant changes to the electronic environment on the surface, and the order of metal deposition was not arbitrary.

These effects were also observed in the XPS regions for Ni 2p, Co 2p, and Ce 3d in Figure 5. The Ni $2p_{3/2}$ binding energy region is shown in Figure 5a; the Ni $2p_{1/2}$ peaks were not detectable because of overlap with the overpowering Ce 3d peaks. Two nickel species were observed, which have been assigned to Ni^{2+}.[53,54] A broad satellite peak was also observed ~860 eV.[53,54]

Nickel deposited onto CeO_2 and calcined resulted in oxidized Ni^{2+}, similar to NiO/CeO_2 (~855.5 eV)[55] and $Ni(OH)_2$ (≥ 858 eV)[54] species for both Ni/CeO_2 and $Ni/Co/CeO_2$, which was assigned based on previous studies on ceria-supported Ni, which describes the tendency of Ni to form hydroxyls on ceria.[53,54] The Ni-hydroxyl peak shifted to lower binding energies once the material was reduced at 450 °C, where it may be attributed to hydroxyls or carbonates.[54]

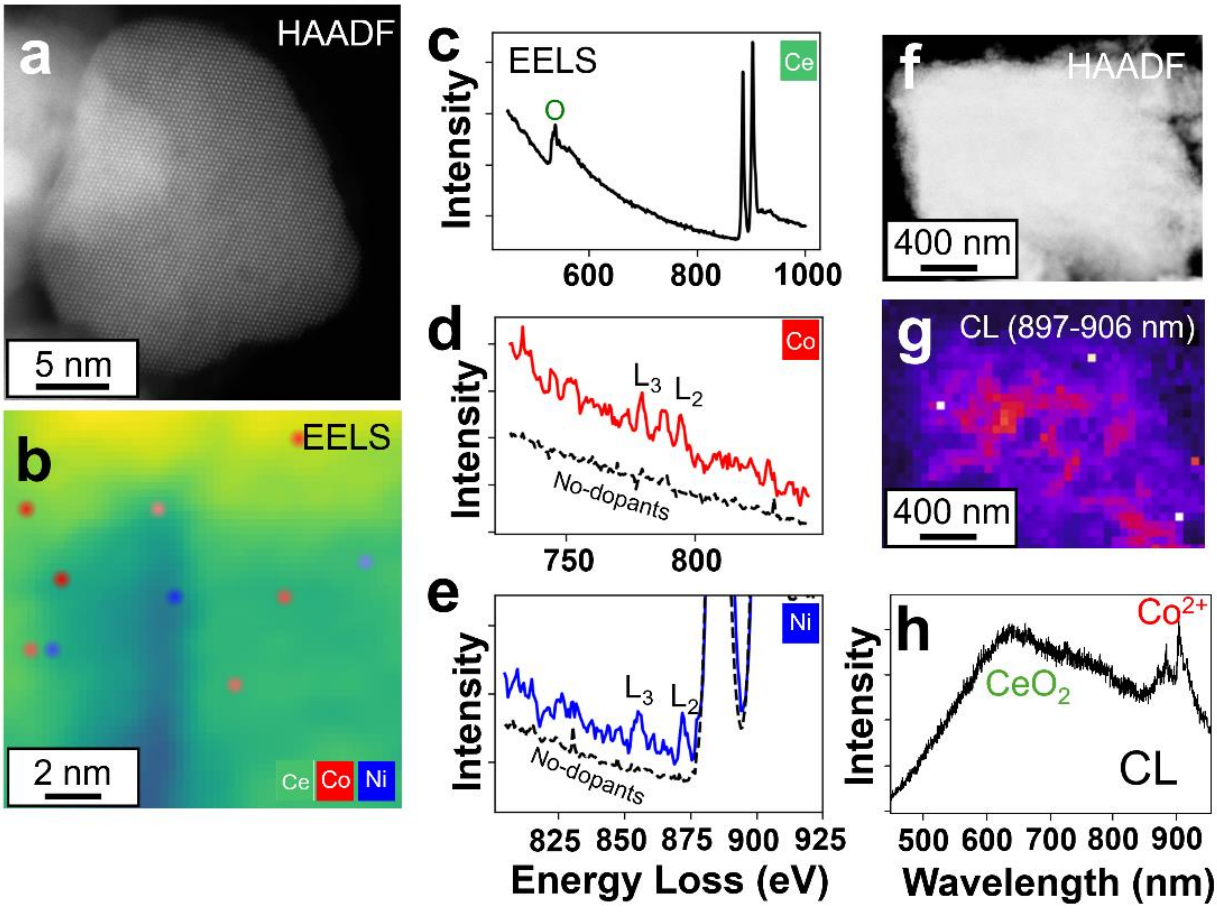

Figure 4. a) HAADF image showing high crystalline CeO_2 nanoparticle, with Co and Ni single atoms grafted onto the surface ($Ni/Co/CeO_2$); b) STEM-EELS mapping of Co and Ni single atoms on CeO_2 nanoparticles; c) EELS spectrum from CeO_2 nanoparticle; d) EELS spectrum from Co single atoms; e) EELS spectrum from Ni single atoms; f) HAADF image and g) corresponding CL mapping of 897-906nm; h) CL spectrum showing a board peak around 650 nm from CeO_2 and two sharp peaks at 880 nm and 900 nm from Co.

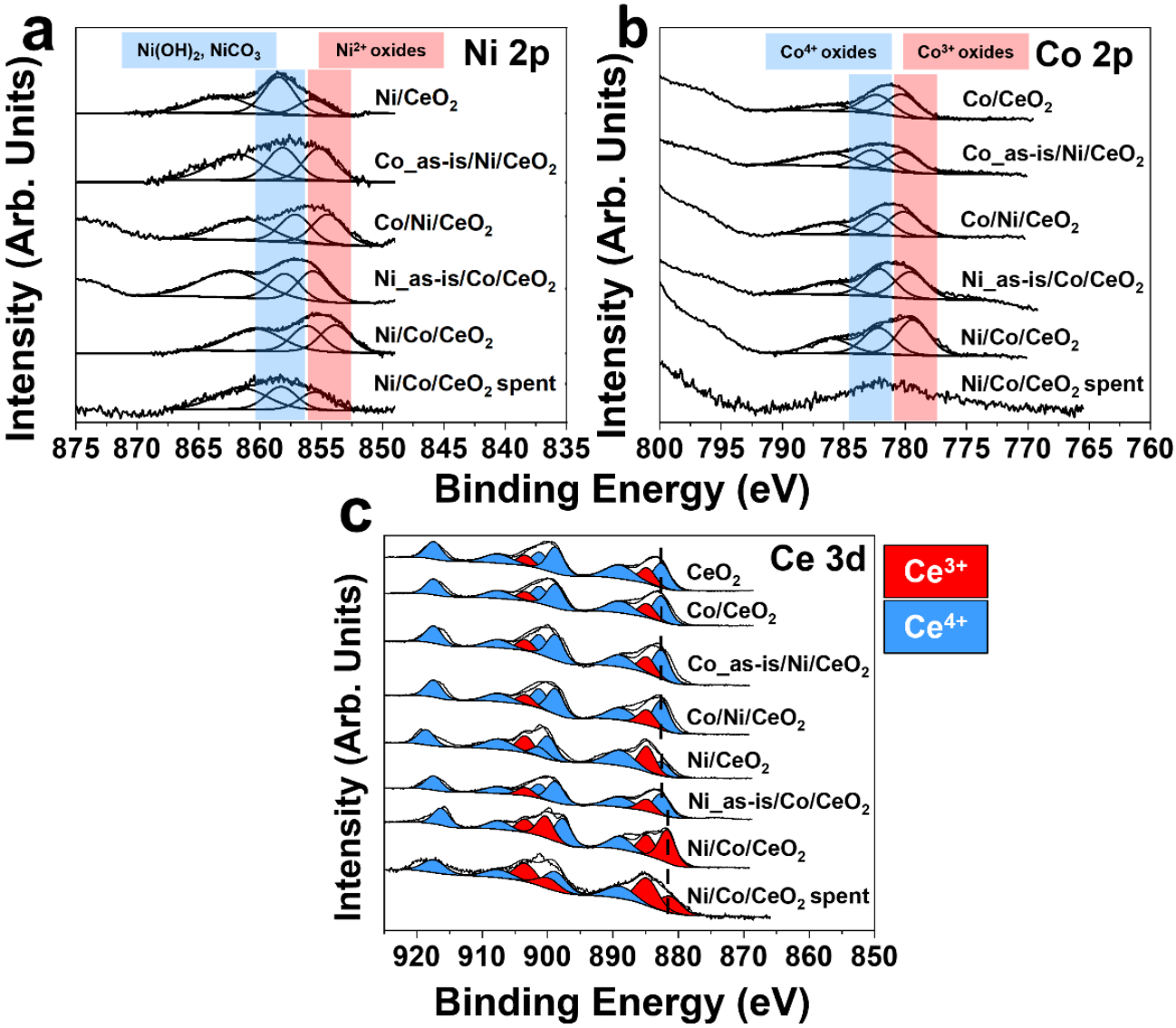

Figure 5. a) XPS of the Ni 2p binding energy region; b) Co 2p binding energy region; and c) Ce 3d binding energy region for CeO_2, Ni/CeO_2 (calcined at 450 °C), Co/CeO_2 (calcined at 450 °C), Co_as-is/Ni/CeO_2 (Ni calcined at 450 ºC, Co added), $Co/Ni/CeO_2$ (Ni calcined at 450 ºC, Co added then reduced in H_2 and transferred to chamber without air exposure), Ni_as-is/Co/CeO_2 (Co calcined at 450 °C, Ni added then reduced in H_2 and transferred to chamber without air exposure), $Ni/Co/CeO_2$ (Co calcined at 450 °C, Ni added then reduced) and $Ni/Co/CeO_2$ spent. More oxidized species are shown in blue and more reduced species are shown in red.

For $Ni/Co/CeO_2$, the oxide Ni^{2+} species shifted significantly to lower binding energies (855.6 eV → 853.8 eV, Δ = +1.2 eV) after reduction in hydrogen. By comparison, on $Co/Ni/CeO_2$ this Ni^{2+} peak shifted less (855.0 eV → 854.4 eV, Δ = +0.6 eV) after reduction, demonstrating that Ni was more easily reduced when Co was deposited first. While this peak shift was significant, the resulting Ni XPS peaks still fall within the binding energy range of the Ni^{2+} oxidation state. No metallic Ni^0 was observed by XPS, even though care was taken not to expose the reduced material to air. Even under the H_2 reduction conditions, Ni was fully not reduced to metal due to support interactions. The charge transfer between Ni and CeO_2 has been widely reported[53,54,56,57] and is described by Eqn. 8.[56]

$$2Ce^{4+} + Ni^0 \leftrightarrow 2Ce^{3+} + Ni^{2+} \quad (8)$$

This redox behavior explains that nickel cannot be fully reduced on CeO_2 and instead forms Ni^{2+} with higher electron density and strong metal-support interactions.[18] Additionally, interactions are enhanced when Ni is in greater contact with CeO_2, as is expected for the single ion sites observed in $Ni/Co/CeO_2$ by TEM in Figure 4. This observation agrees with a recent study by Barreau et al.,[49] who suggested that the metallic Ni active site was not required for CO_2 methanation. Instead, small ionic NiO clusters (~2 nm) embedded in CeO_2 were shown to be active in their study.

The relationship between the Ni oxidation state and methanation activity has been studied in detail by Barreau et al. with *in-situ* soft X-ray absorption spectroscopy (sXAS) experiments.[49] These analyses showed that under CO_2, Ni was oxidized to a $NiO/Ni^{\delta+}$ - Ce^{3+} mixed state, with NiO eventually reduced to Ni^0 at higher temperatures and $Ni^{\delta+}$ - Ce^{3+} remaining. The authors theorized that these redox Ni/Ce pairs

were the primary active sites for CO_2 methanation. These findings are congruent with the present study, which found that Ni was likely in an oxidized state for the duration of the methanation reaction (Figure 5a), while the methane yield was able to achieve 80% for the duration of the test (Figure 3).

The spent Ni/Co/CeO_2 catalyst showed more oxidized Ni 2p peaks, as expected due to re-exposure to air, so any Ni oxidation *in-situ* cannot be determined from XPS.

The Co $2p_{3/2}$ binding energy regions in Figure 5b reveal Co^{2+} (780.1 eV),[58,59] Co^{3+} (779.0 eV)[59] and $Co(OH)_2$ (781.6 - 782.2 eV)[58,59] species on CeO_2, while the Co $2p_{1/2}$ peaks were hidden by the Ce LMM peak at 830 eV.[60] The Co^{3+} was slightly reduced when Ni was deposited onto calcined Co/CeO_2, evidenced by a +0.6 eV shift compared to calcined Co/CeO_2 alone. However, this shift was not observed when Co was added to calcined Ni/CeO_2 (Figure 5b). This confirms the importance of metal deposition order on catalyst properties, with Co/CeO_2 acting as a new support material and facilitating electronic interactions with Ni. For Ni/Co/CeO_2, the Co^{2+} peak was not significantly shifted after reduction, and no metallic Co^0 was observed on any samples, even after reduction. This could theoretically be attributed to redox interactions between Co and CeO_2, but this was not observed in the present study.

Analysis of the Ce 3d binding energy regions, shown in Figure 5c, can shed light on the electron transfer between adatoms and CeO_2. However, the Ce 3d signature is complicated and challenging to fit, meaning that choices in fitting parameters and peak assignments can vary between studies of similar spectra. The Ce 3d binding energy peaks are so distinct, they have unique designations. These are *v* (Ce $3d_{5/2}$, 4+), *v'* (Ce $3d_{5/2}$, 3+), *v''* (Ce $3d_{5/2}$, 4+), *v'''* (Ce $3d_{5/2}$, 4+), *u* (Ce $3d_{3/2}$, 4+), *u'* (Ce 3d3/2 3+), *u''* (Ce $3d_{3/2}$, 4+), and *u'''* (Ce $3d_{3/2}$, 4+).[54,61] Additionally, another Ce^{3+} species may be present at lower binding energy, denoted as v^0 (Ce $3d_{5/2}$, 3+) and u^0 (Ce $3d_{3/2}$, 3+).[54] In this work, all Ce 3d peaks were fit with spin-orbit splitting of 18.6 eV, and corresponding peaks between samples were constrained to the same binding energy positions and peak FWHM as those in the bare CeO_2, except when the fit was deemed insufficient because the peak binding energy had shifted. In Figure 5c, the peaks assigned to Ce^{4+} are shaded in blue, and the peaks assigned to Ce^{3+} are shaded in red. These peak areas were used to determine the Ce^{3+}/Ce^{4+} ratio shown in Table 4.

Table 4. Calculated ratios of Ce^{3+}/Ce^{4+} by XPS of the Ce 3d region in Figure 5.

Sample	Ce^{3+}/Ce^{4+}
CeO_2	0.26
Co/CeO_2 (calcined at 450 °C)	0.24
Ni_as-is/Co/CeO_2	0.24
Ni/Co/CeO_2 (reduced)	1.16
Ni/Co/CeO_2 (spent)	0.99
Ni/CeO_2 (calcined at 450 °C)	0.41
Co_as-is/Ni/CeO_2	0.24
Co/Ni/CeO_2 (reduced)	0.31

The expected Ce^{3+} $3d_{5/2}$ peak in CeO_2 was assigned to 884.8 eV (*v'*) and was present on all samples. The Ce^{4+} $3d_{5/2}$ peaks were found at 882.6 eV (v), 888.9 eV (*v''*), and 901.2 eV (*v'''*). The *v''* and *v'''* peaks were observed on all samples, while the *v* peak was found on all samples except for Ni/Co/CeO_2 before and after methanation. For these samples, the *v* peak had been reduced to an additional Ce^{3+} peak (v^0) at 881.3 eV.[54] Charge from the Ni and Co adatoms redistributes towards neighboring oxygen and cerium atoms, where cerium atoms are reduced [$Ce^{4+} \rightarrow Ce^{3+}$] by coordination to the electron-rich $Ni^{\delta+}$ state. The ratios of Ce^{3+} to Ce^{4+} are shown in Table 4. Untreated CeO_2 had a Ce^{3+}/Ce^{4+} ratio = 0.26, which increased to 0.41 when Ni was added and calcined at 450 °C but was unchanged by Co addition (after calcination) (0.24). This charge transfer was observed by the increase of the Ce^{3+}/Ce^{4+} ratio on Ni/Co/CeO_2 catalyst after reduction (1.16). The abundance of Ce^{3+} sites on Ni/Co/CeO_2 indicates increased interaction with oxidized Ni and the prevalence of

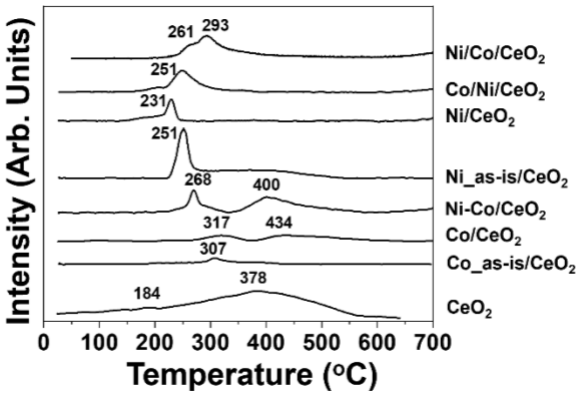

Figure 6. H_2-TPR of CeO_2, Co_as-is/CeO_2, Co/CeO_2 (calcined at 450 °C), Ni-Co/CeO_2 (Ni deposited on calcined Co/CeO_2), Ni_as-is/CeO_2, Ni/CeO_2 (calcined at 450 °C), Co/Ni/CeO_2 (Co deposited on calcined Ni/CeO_2) and Ni-Co/CeO_2 (Co deposited then Ni, drying step in between).

$Ni^{\delta+}$ - Ce^{3+} active sites. This redox interaction between Ni and CeO_2 supports both H_2 dissociation and CO_2 activation for methane formation.[49] The charge transfer also creates oxygen vacancies, which in turn increases the adsorption of the atoms and hence its stability against sintering.[62,63]

To support that this observation was caused by Ni/Ce redox interactions and not simply catalyst reduction in H_2, as well as investigating the importance of deposition order, the Ce^{3+}/Ce^{4+} ratio was determined for reduced Co/Ni/CeO_2 catalyst as well (Ni deposited first, Co second), shown in Table 4. The Ce^{3+}/Ce^{4+} ratio for Co/Ni was much lower than Ni/Co at only 0.31, proving both that the H_2 reduction step was not solely responsible for reducing Ce^{4+} to Ce^{3+} and that the Ce reduction was more favorable when Co was deposited first. This was notable because Co by itself does not facilitate Ce charge transfer, pointing to a bimetallic synergetic interaction between Ni and Co/CeO_2 support. In the spent Ni/Co/CeO_2, the ceria remains partly reduced even after re-exposure to air, confirming that the charge transfer is due to the addition of the Ni onto Co/CeO_2.

H_2-TPR experiments were carried out for CeO_2, as prepared Co_as-is/CeO_2, Ni_as-is/CeO_2, and Ni-Co/CeO_2 (without any prior heat treatment) as well as Co/CeO_2 and Ni/Co/CeO_2 which were calcined (450 °C 2 h air) after the deposition of Co, and Ni/CeO_2 and Co/Ni/CeO_2 which was calcined (450 °C 2 h air) after the deposition of Ni, to elucidate the reduction temperature, the overall reducibility below the pre-activation temperature (500 °C) and whether they are interactions between Ni, Co and ceria (Figure 6). A wide but weak reduction peak of CeO_2 occurs at 184 and 378 °C, corresponding to the reduction of CeO_2 and can be attributed

to adsorbed oxygen species and lattice oxygen species, respectively.[64] For the as-prepared Co/CeO_2 there is one peak at 307 °C, while for the calcined Co/CeO_2, there are two peaks at 317 °C and 434 °C corresponding to reduction of Co^{3+} to Co^{2+} and Co^{2+} to Co^0.[65] Upon addition of Ni on CeO_2, the reduction temperature of ceria is shifted to lower temperatures and the reducibility is enhanced. It should be noted that Ni reduction peaks do not describe full reduction to metal, which was not observed by XPS in Figure 5a. In a study by Li et al., the authors described H_2-TPR reduction peaks for Ni/CeO_2 between 225 ºC and 290 ºC, which were attributed to the reduction of reactive oxygen species generated by the redox formation of Ni-O-Ce solid solution.[66] The main reduction peak on Ni/CeO_2 observed at 251 °C corresponds to the Ni-O-Ce peaks described by Li et. al.[66] When Ni is deposited on Co/CeO_2 (after calcination), there are 2 reduction peaks (261 and 293 °C) corresponding to the reactive oxygens formed by Ni-O-Ce and partial reduction of Co species, respectively. The reduction of Co species shifted to lower temperature (317 to 293 °C) compared to Co/CeO_2, while that of Ni shifted to higher temperature (231 to 261 °C), compared to Ni/CeO_2 indicating strong interactions between Ni and Co species. On $Co/Ni/CeO_2$, the reduction corresponding to Co is barely visible as the only reduction peak is at the same temperature as for Ni/CeO_2. For Ni-Co, the peak and the shoulder at 268 °C corresponds to the reactive oxygens formed by Ni-O-Ce and partial reduction of Co, respectively but the wide peak centered at 400 °C indicates strong interactions of Ni and/or Co species with ceria. The hydrogen consumption increases in that order Ni-Co = Co/Ni < Ni < Co < Co_as-is < Ni_as-is< Ni/Co (Table 5). H_2 consumption that is higher than 1 mol H_2 per mol of metal, indicates that surface ceria is being reduced due to strong metal-support interactions. The high reducibility of the $Ni/Co/CeO_2$ catalyst and the enhanced interactions of Ni with ceria are in agreement with XPS analysis (*vide supra*, Table 4).

Table 5. Results from TPR-H_2 experiment.

Sample	Peak Temp (°C)	mol H_2/ mol (Ni + Co)
Co_as-is/CeO_2	307	13.1
Co/CeO_2	317/434	11.6
Ni/Co/CeO_2	266/293	22.2
Ni_as-is/CeO_2	251/367	17.2
Ni/CeO_2	231	1.5
Co/Ni/CeO_2	251	1.3
Ni-Co/CeO_2	268/400	1.3

The Ni active site is known for the dissociation of H_2, while the surface must also facilitate CO_2 adsorption and activation onto the metal oxide support.[21] CO_2 is weakly acidic, therefore surface basic sites facilitate adsorption. Hence CO_2 temperature programmed desorption (CO_2-TPD) can determine which sites activate CO_2 adsorption. In Figure 7, the CO_2-TPD is shown for CeO_2, Co_as-is/CeO_2, Co/CeO_2 (after calcination), Ni_as-is/CeO_2, Ni/CeO_2 (after calcination), Ni-Co/CeO_2, $Co/Ni/CeO_2$ (Co deposited on calcined Ni/CeO_2), and $Ni/Co/CeO_2$ (Ni deposited on calcined Co/CeO_2) to compare the CO_2 activation. According to literature, three types of basic sites can be distinguished depending on the CO_2 desorption temperature: weak, medium and strong. The weak one corresponds to weakly bonded

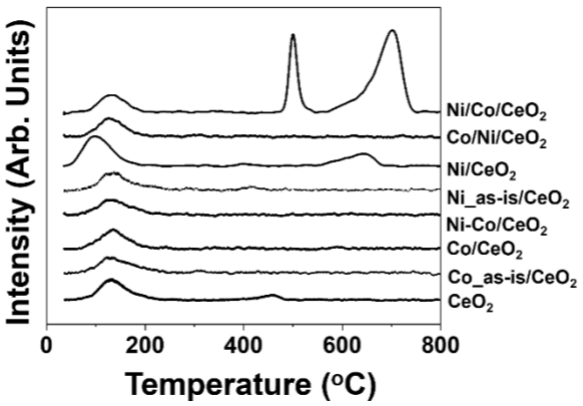

Figure 7. TPD-CO_2 of CeO_2, Co_as-is/CeO_2, Co/CeO_2 (calcined at 450 °C), $Ni/Co/CeO_2$ (Ni deposited on calcined Co/CeO_2), Ni_as-is/CeO_2, $Co/Ni/CeO_2$ (Co deposited on calcined Ni/CeO_2) and Ni-Co/CeO_2 (Co deposited then Ni, drying step in between). All samples are subjected to *in-situ* reduction at 500 °C prior TPD-CO_2.

bicarbonate species onto Brønstead OH groups. The medium basic sites, specifically metal oxygen pairs on the catalyst surface (metal-O_2^-), and the strong basic sites are related to Lewis basic sites. The temperature of each peak reported in literature may vary; the maximum temperature corresponding to the weak sites can vary between 150 - 300 °C, the medium sites between 300-500 °C and the strong sites above 500 or even 700 °C.[21,67] Weak and moderate basic sites of support materials favor the activation of CO_2[40,68] and are more crucial for methanation,[69] as CO_2 adsorbed too strongly would be hard to desorb and cannot participate in CO_2 activation. While all the samples show the low temperature peak as observed in the CeO_2 support, only Ni/Co shows CO_2 desorption peaks at medium and higher temperatures, and monometallic Ni had only one small peak at high temperatures, indicating that the specific interaction between CeO_2, Ni, and Co in Ni/Co is more likely to adsorb CO_2 strongly. The number of moles of CO_2 per total moles of metals that were desorbed from each material was quantified. Calibrated to a standard CO_2 pulse without catalyst, the moles of CO_2 were calculated, and the total uptake of CO_2 per gram of catalyst was determined (Table S3). The $Ni/Co/CeO_2$ catalyst had a significantly higher CO_2 adsorption uptake compared to the Ni/CeO_2 catalyst (Table S3) indicating a higher density of basic sites, leading to higher catalytic performance for CO_2 methanation.[70]

Computational modeling of Ni and Co on CeO_2. A computational investigation was conducted to examine the structures and charges of the Ni/CeO_2 and $Ni/Co/CeO_2$ systems. In the DFT-optimized structure of Ni/CeO_2 (Figure 8a), the nickel atom is coordinated by two oxygen atoms from the CeO_2 surface. Two potential geometries were optimized for $Ni/Co/CeO_2$, with one shown in Figure 8b and the other reported in the Supporting Information (Figure S10, Table S4). In the $Ni/Co/CeO_2$ catalyst (Figure 8b), both nickel and cobalt atoms are coordinated by two surface oxygen atoms, with one oxygen atom being shared between the two metals. To evaluate the influence of cobalt on the electronic structure, Bader charge analysis was performed (Table 6). The Bader charge of cerium was computed as the average over all cerium

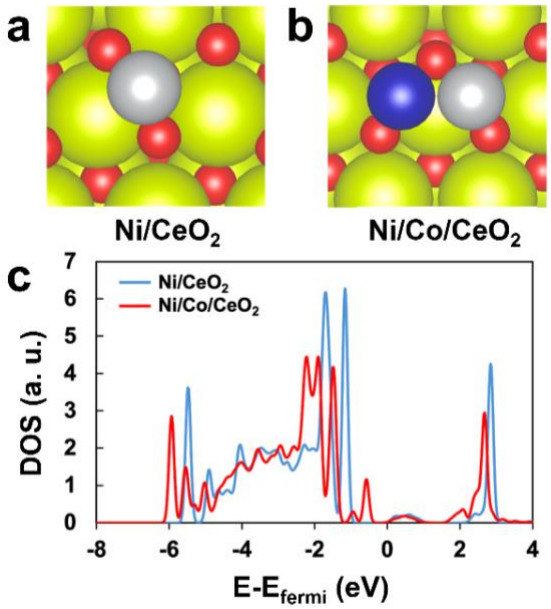

Figure 8. (a) Top view of the optimized geometry of Ni/CeO_2. (b) Top view of the optimized geometry of $Ni/Co/CeO_2$. Color scheme: cerium (yellow), oxygen (red), nickel (silver), and cobalt (blue). (c) Projected density of states (PDOS) of the Ni *3d* orbitals in Ni/CeO_2 (blue) and $Ni/Co/CeO_2$ (red).

atoms in the structure. The results show that both nickel and cerium exhibit lower Bader charges in the $Ni/Co/CeO_2$ system, indicating that the presence of cobalt enhances the reduction of both Ni and Ce through electronic interactions.

Table 6. Bader charges of Ni, Co, and Ce atoms in Ni/CeO_2 and $Ni/Co/CeO_2$ catalysts. The Bader charge of Ce is reported as the average over all cerium atoms in the system.

Bader charge	Ni	Co	Ce
Ni/CeO_2	0.57	N/A	2.37
$Ni/Co/CeO_2$	0.51	0.63	2.35

The density of states (DOS) profile of the Ni 3d orbitals (Figure 8c) reveals distinct electronic differences between the Ni/CeO_2 and $Ni/Co/CeO_2$ systems. In $Ni/Co/CeO_2$, the DOS exhibits a pronounced shift toward lower energies, indicating a more reduced state of nickel compared to that in Ni/CeO_2. This shift corresponds to an increased occupancy of the Ni 3d states. These results suggest that the incorporation of cobalt facilitates electron transfer or alters the local electronic structure, thereby enhancing the electron density at the Ni site. Consequently, the presence of cobalt plays a critical role in tuning the redox properties and potentially the catalytic activity of the Ni species. These theoretical results agree well with experimental XPS results, in which Ni was more reduced when deposited onto Co/CeO_2 (Figure 5a) and resulted in the highest Ce^{3+}/Ce^{4+} ratio (Table 4).

Conclusions

The organometallic grafting synthesis is used to prepare 27 different combinations of Ni and additives such as B, Cu, Co, Fe, Mn, Sn, Mg, V, and Zn and oxide-supports including Al_2O_3, CeO_2, and SiO_2 for the CO_2 methanation reaction. 0.16 % Ni / 0.15 % Co / CeO_2, with Co added first, calcined at 450 °C, followed by addition of Ni, was found to be the most active catalyst with a CO_2 conversion of 84.3 % and methane selectivity of 99.6 % at 300 °C at $H_2/CO_2 = 4.0$ with an *in-situ* pre-reduction at 500 °C in 10 % H_2. High-resolution TEM images showed the presence of single atoms which prevailed after 15 h reaction. X-ray photoelectron spectroscopy shows that the $Ni^{\delta+}$ - Ce^{3+} redox pair was formed on $Ni/Co/CeO_2$, while Co increased the electron density around Ni. This $Ni/Co/CeO_2$ combination had improved reducibility and increased basic sites, compared to Ni/CeO_2, Co/CeO_2, $Ni\text{-}Co/CeO_2$ and $Co/Ni/CeO_2$, as observed by H_2-temperature-programmed reduction and CO_2-temperature-programed desorption, respectively. Density functional theory calculations supported these results, which observed that the calculated Bader charge on Ni was decreased when Co is present for $Ni\text{-}O\text{-}Co/CeO_2$. These results suggest that Ni gained electron density when deposited onto Co/CeO_2, which acted as a new support material working synergistically with Ni active sites. This study shows that ultra-low loading of single cationic Ni on Co/CeO_2 support can be highly active and stable for the methanation reaction.

ASSOCIATED CONTENT

Supporting Information. DFT experimental methods, surface area, equilibrium calculations, XRD, TGA, and additional HRTEM images. This material is available free of charge via the Internet at http://pubs.acs.org.XXXX.

AUTHOR INFORMATION

Corresponding Authors

Magali S. Ferrandon - *Chemical Sciences and Engineering Division, Argonne National Laboratory, Lemont, Illinois 60439, United States;* orcid.org/0000-0003-2544-6466 Email: ferrandon@anl.gov

Jianguo Wen - *Center for Nanoscale Materials Argonne National Laboratory, Argonne, Lemont, Illinois 60439, United States;* orcid.org/0000-0002-3755-0044; Email: jwen@anl.gov

Massimiliano Delferro - *Chemical Sciences and Engineering Division, Argonne National Laboratory, Lemont, Illinois 60439, United States;* orcid.org/0000-0002-4443-165X; Email: delferro@anl.gov

Authors

Carly Byron - *Chemical Sciences and Engineering Division, Argonne National Laboratory, Lemont, Illinois 60439, United States;* orcid.org/0000-0002-1716-5659; Email: cbyron@anl.gov

Yu Lim Kim - *Chemical Sciences and Engineering Division, Argonne National Laboratory, Lemont, Illinois 60439, United States;* orcid.org/0009-0009-8138-5849; Email: yu.kim@anl.gov

Jacob T. Bryant - *Chemical Sciences and Engineering Division, Argonne National Laboratory, Lemont, Illinois 60439, United States;* orcid.org/0000-0002-7737-4604; Email: bryantj@anl.gov

Jacklyn N. Hall - *Chemical Sciences and Engineering Division, Argonne National Laboratory, Lemont, Illinois 60439, United States;* orcid.org/0000-0003-4960-1344; Email: jnhall@anl.gov

Tao Zhou- *Center for Nanoscale Materials, Argonne National Laboratory, Lemont, Illinois 60439, United States;* orcid.org/0000-0002-8093-7666; Email: tzhou@anl.gov

Cong Liu - *Chemical Sciences and Engineering Division, Argonne National Laboratory, Lemont, Illinois 60439, United States;* orcid.org/0000-0002-2145-5034; Email: congliu@anl.gov

Author Contributions

The manuscript was written through contributions of all authors. All authors have given approval to the final version of the manuscript.

Funding Sources

Work at Argonne National Laboratory was supported by the U.S. Department of Energy (DOE), Office of Basic Energy Sciences, Division of Chemical Sciences, Geosciences, and Biosciences, Catalysis Science Program under contract No. DE-AC-02-06CH11357. Work performed at the Center for Nanoscale Materials, a U.S. Department of Energy Office of Science User Facility, was supported by the U.S. DOE, Office of Basic Energy Sciences, under Contract No. DE-AC02-06CH11357.

REFERENCES

(1) Strucks, P.; Failing, L.; Kaluza, S. A Short Review on Ni-Catalyzed Methanation of CO_2: Reaction Mechanism, Catalyst Deactivation, Dynamic Operation. *Chem. Ing. Tech.* **2021**, *93*, 1526–1536.

(2) Götz, M.; Lefebvre, J.; Mörs, F.; McDaniel Koch, A.; Graf, F.; Bajohr, S.; Reimert, R.; Kolb, T. Renewable Power-to-Gas: A Technological and Economic Review. *Renewable Energy* **2016**, *85*, 1371–1390.

(3) Frontera, P.; Macario, A.; Ferraro, M.; Antonucci, P. Supported Catalysts for CO_2 Methanation: A Review. *Catalysts* **2017**, *7*, 59.

(4) Ashok, J.; Pati, S.; Hongmanorom, P.; Tianxi, Z.; Junmei, C.; Kawi, S. A Review of Recent Catalyst Advances in CO_2 Methanation Processes. *Catal. Today* **2020**, *356*, 471–489.

(5) Li, S.; Xu, Y.; Chen, Y.; Li, W.; Lin, L.; Li, M.; Deng, Y.; Wang, X.; Ge, B.; Yang, C.; Yao, S.; Xie, J.; Li, Y.; Liu, X.; Ma, D. Tuning the Selectivity of Catalytic Carbon Dioxide Hydrogenation over Iridium/Cerium Oxide Catalysts with a Strong Metal–Support Interaction. *Angew. Chem.* **2017**, *129*, 10901–10905.

(6) Wang, X.; Shi, H.; Kwak, J. H.; Szanyi, J. Mechanism of CO_2 Hydrogenation on Pd/Al_2O_3 Catalysts: Kinetics and Transient DRIFTS-MS Studies. *ACS Catal.* **2015**, *5*, 6337–6349.

(7) Karelovic, A.; Ruiz, P. Mechanistic Study of Low Temperature CO_2 Methanation over Rh/TiO_2 Catalysts. *J. Catal.* **2013**, *301*, 141–153.

(8) Sharma, S.; Hu, Z.; Zhang, P.; McFarland, E. W.; Metiu, H. CO_2 Methanation on Ru-Doped Ceria. *J. Catal.* **2011**, *278*, 297–309.

(9) Alrafei, B.; Polaert, I.; Ledoux, A.; Azzolina-Jury, F. Remarkably Stable and Efficient Ni and Ni-Co Catalysts for CO_2 Methanation. *Catal. Today* **2020**, *346*, 23–33.

(10) Kim, J. Ni Catalysts for Thermochemical CO_2 Methanation: A Review. *Coatings* **2024**, *14*, 1322.

(11) Ren, J.; Qin, X.; Yang, J.-Z.; Qin, Z.-F.; Guo, H.-L.; Lin, J.-Y.; Li, Z. Methanation of Carbon Dioxide over Ni–M/ZrO_2 (M=Fe, Co, Cu) Catalysts: Effect of Addition of a Second Metal. *Fuel Process. Technol.* **2015**, *137*, 204–211.

(12) Burger, T.; Koschany, F.; Thomys, O.; Köhler, K.; Hinrichsen, O. CO_2 Methanation over Fe- and Mn-Promoted Co-Precipitated Ni-Al Catalysts: Synthesis, Characterization and Catalysis Study. *Appl. Catal., A* **2018**, *558*, 44-54.

(13) Wang, W.; Zhang, J.; Fan, G.; Li, F. Defect-Rich and Boron-Doped Al_2O_3-Supported Ru Nanocatalyst for Enhanced CO_2 Methanation Activity. *Energy Fuels* **2023**, *37*, 8386–8397.

(14) Bacariza, M. C.; Graça, I.; Bebiano, S. S.; Lopes, J. M.; Henriques, C. Magnesium as Promoter of CO_2 Methanation on Ni-Based USY Zeolites. *Energy Fuels* **2017**, *31*, 9776–9789.

(15) Garbarino, G.; Wang, C.; Cavattoni, T.; Finocchio, E.; Riani, P.; Flytzani-Stephanopoulos, M.; Busca, G. A Study of Ni/La-Al_2O_3 Catalysts: A Competitive System for CO_2 Methanation. *Appl. Catal., B* **2019**, *248*, 286–297.

(16) Le, T. A.; Kim, M. S.; Lee, S. H.; Kim, T. W.; Park, E. D. CO and CO_2 Methanation over Supported Ni Catalysts. *Catal. Today* **2017**, *293–294*, 89–96.

(17) Zhou, R.; Rui, N.; Fan, Z.; Liu, C. Effect of the Structure of Ni/TiO_2 Catalyst on CO_2 Methanation. *Int. J. Hydrogen Energy* **2016**, *41*, 22017–22025.

(18) Lin, S.; Tang, R.; Liu, X.; Gong, L.; Li, Z. Modulating CO_2 Methanation Activity on Ni/CeO_2 Catalysts by Tuning Ceria Facet-Induced Metal-Support Interaction. *Int. J. Hydrogen Energy* **2024**, *51*, 462–475.

(19) Kenyotha, K.; Kidkhunthod, P.; Poo-arporn, Y.; Chanapattharapol, K. C. Ceria-Supported Ni Catalyst with High Catalytic Activity, Selectivity and Stability for CO_2 Conversion to CH_4 by Hydrogenation Reaction Investigated by X-Ray Absorption Spectroscopy. *J. Phys. Chem. Solids* **2024**, *190*, -112009.

(20) Zou, X. Shen, Z.; Li, X.; Cao, Y.; Xia, Q.; Zhang, S.; Liu, Y.; Jiang, L.; Li, L.; Cui, L.; Wang, Y. Boosting CO_2 Methanation on Ceria Supported Transition Metal Catalysts via Chelation Coupled Wetness Impregnation. *J. Colloid. InterfaceSci.* **2022**, *620*, 77-85.

(21) Kuhaudomlap, S.; Srifa, A.; Koo-Amornpattana, W.; Fukuhara, C.; Ratchahat, S. Insight and Comprehensive Study of Ni-Based Catalysts Supported on Various Metal Oxides for CO_2 Methanation. *Sci. Rep.* **2024**, *14*, 23149.

(22) Serafin, J.; Llorca, J. Nanoshaped Cerium Oxide with Nickel as a Non-Noble Metal Catalyst for CO_2 Thermochemical Reactions. *Molecules* **2023**, *28*, 2926.

(23) Akri, M.; Zhao, S.; Li, X.; Zang, K.; Lee, A. F.; Isaacs, M. A.; Xi, W.; Gangarajula, Y.; Luo, J.; Ren, Y.; Cui, Y.-T.; Li, L.; Su, Y.; Pan, X.; Wen, W.; Pan, Y.; Wilson, K.; Li, L.; Qiao, B.; Ishii, H.; Liao, Y.-F.; Wang, A.; Wang, X.; Zhang, T. Atomically Dispersed Nickel as Coke-Resistant Active Sites for Methane Dry Reforming. *Nat. Commun.* **2019**, *10*, 5181.

(24) Garbarino, G.; Riani, P.; Magistri, L.; Busca, G. A Study of the Methanation of Carbon Dioxide on Ni/Al_2O_3 Catalysts at Atmospheric Pressure. *Int. J. Hydrogen Energy* **2014**, *39*, 11557–11565.

(25) Wei, L.; Grénman, H.; Haije, W.; Kumar, N.; Aho, A.; Eränen, K.; Wei, L.; De Jong, W. Sub-Nanometer Ceria-Promoted Ni 13X Zeolite Catalyst for CO_2 Methanation. *Appl. Catal., A* **2021**, *612*, 118012.

(26) Gonçalves, L. P. L.; Mielby, J.; Soares, O. S. G. P.; Sousa, J. P. S.; Petrovykh, D. Y.; Lebedev, O. I.; Pereira, M. F. R.; Kegnæs, S.; Kolen'ko, Y. V. In Situ Investigation of the CO_2 Methanation on Carbon/Ceria-Supported Ni Catalysts Using Modulation-Excitation DRIFTS. *Appl. Catal., B* **2022**, *312*, 121376.

(27) Deng, L.; Liu, X.; Wang, R.; Wang, C.; Zhou, G. Unsupported Ni-Co Alloy as Efficient Catalysts for CO_2 Methanation. *J. Alloys Compd.* **2022**, *918*, 165472.

(28) Copéret, C.; Comas-Vives, A.; Conley, M. P.; Estes, D. P.; Fedorov, A.; Mougel, V.; Nagae, H.; Núñez-Zarur, F.; Zhizhko,

P. A. Surface Organometallic and Coordination Chemistry toward Single-Site Heterogeneous Catalysts: Strategies, Methods, Structures, and Activities. *Chem. Rev.* **2016**, *116*, 323–421.

(29) Mavrokefalos, C. K.; Kaeffer, N.; Liu, H.-J.; Krumeich, F.; Copéret, C. Small and Narrowly Distributed Copper Nanoparticles Supported on Carbon Prepared by Surface Organometallic Chemistry for Selective Hydrogenation and CO_2 Electroconversion Processes. *ChemCatChem* **2020**, *12*, 305-313

(30) Ligthart, D. A. J. M.; Van Santen, R. A.; Hensen, E. J. M. Influence of Particle Size on the Activity and Stability in Steam Methane Reforming of Supported Rh Nanoparticles. *J. Catal.* **2011**, *280*, 206–220.

(31) McCullough, K. E.; King, D. S.; Chheda, S. P.; Ferrandon, M. S.; Goetjen, T. A.; Syed, Z. H.; Graham, T. R.; Washton, N. M.; Farha, O. K.; Gagliardi, L.; Delferro, M. High-Throughput Experimentation, Theoretical Modeling, and Human Intuition: Lessons Learned in Metal–Organic-Framework-Supported Catalyst Design. *ACS Cent. Sci.* **2023**, *9*, 266–276.

(32) Kort-Kamp, W. J. M.; Ferrandon, M.; Wang, X.; Park, J. H.; Malla, R. K.; Ahmed, T.; Holby, E. F.; Myers, D. J.; Zelenay, P. Adaptive Learning-Driven High-Throughput Synthesis of Oxygen Reduction Reaction Fe–N–C Electrocatalysts. *J. Power Sources* **2023**, *559*, 232583.

(33) Ferrandon, M. S.; Byron, C.; Celik, G.; Zhang, Y.; Ni, C.; Sloppy, J.; McCormick, R. A.; Booksh, K.; Teplyakov, A. V.; Delferro, M. Grafted Nickel-Promoter Catalysts for Dry Reforming of Methane Identified through High-Throughput Experimentation. *Appl. Catal., A* **2022**, *629*, 118379.

(34) Byron, C.; Leon, P. A. I.; Bryant, J.; Langeslay, R.; Savereide, L.; Wen, J.; Camacho-Bunquin, J.; Notestein, J. M.; Delferro, M.; Ferrandon, M. Single-Atom Manganese-Based Catalysts for the Oxidative Dehydrogenation of Propane. *ACS Catal.* **2024**, *14*, 16698-16711.

(35) Świrk Da Costa, K.; Summa, P.; Wierzbicki, D.; Motak, M.; Da Costa, P. Vanadium Promoted Ni(Mg,Al)O Hydrotalcite-Derived Catalysts for CO_2 Methanation. *Int. J. Hydrogen Energy* **2021**, *46*, 17776–17783.

(36) Vrijburg, W. L.; Moioli, E.; Chen, W.; Zhang, M.; Terlingen, B. J. P.; Zijlstra, B.; Filot, I. A. W.; Züttel, A.; Pidko, E. A.; Hensen, E. J. M. Efficient Base-Metal NiMn/TiO_2 Catalyst for CO_2 Methanation. *ACS Catal.* **2019**, *9*, 7823-7839.

(37) Jiang, Y.; Huang, T.; Dong, L.; Su, T.; Li, B.; Luo, X.; Xie, X.; Qin, Z.; Xu, C.; Ji, H. Mn Modified Ni/Bentonite for CO_2 Methanation. *Catalysts* **2018**, *8*, 646.

(38) Xu, L.; Lian, X.; Chen, M.; Cui, Y.; Wang, F.; Li, W.; Huang, B. CO_2 Methanation over CoNi Bimetal-Doped Ordered Mesoporous Al_2O_3 Catalysts with Enhanced Low-Temperature Activities. *Int. J. Hydrogen Energy* **2018**, *43*, 17172–17184.

(39) Aziz, F. F. A.; Timmiati, S. N.; Jalil, A. A.; Rusdan, N. A.; Annuar, N. H. R.; Teh, L. P. Recent Innovation on Heterogeneous ZnO-Based Catalysts for Enhanced CO_2 Hydrogenation. *J. Environ. Chem. Eng.* **2024**, *12*, 112976.

(40) Byron, C.; Ferrandon, M. S.; Kropf, A. J.; Delferro, M.; Teplyakov, A. V. Surface Basic Site Effect on Boron-Promoted Platinum Catalysts for Dry Reforming of Methane. *J. Phys. Chem. C* **2023**, *127*, 24137–24148.

(41) Vivanco, M.; Ruiz, J.; Floriani, C.; Chiesi-Villa, A.; Rizzoli, C. Chemistry of the Vanadium-Carbon σ Bond. 1. Insertion of Carbon Monoxide, Isocyanides, Carbon Dioxide, and Heterocumulenes into the V-C Bond of Tris(Mesityl)Vanadium(III). *Organometallics* **1993**, *12*, 1794–1801.

(42) Klose, A.; Solari, E.; Floriani, C.; Chiesi-Villa, A.; Rizzoli, C.; Re, N. Magnetic Properties Diagnostic for the Existence of Iron(II)-Iron(II) Bonds in Dinuclear Complexes Which Derive from Stepwise Insertion Reactions on Unsupported Iron-Aryl Bonds. *J. Am. Chem. Soc.* **1994**, *116*, 9123–9135.

(43) Schneider, C. A.; Rasband, W. S.; Eliceiri, K. W. NIH Image to ImageJ: 25 Years of Image Analysis. *Nat. Methods* **2012**, *9*, 671–675.

(44) Gammon, W. J.; Kraft, O.; Reilly, A. C.; Holloway, B. C. Experimental Comparison of N(1s) X-Ray Photoelectron Spectroscopy Binding Energies of Hard and Elastic Amorphous Carbon Nitride Films with Reference Organic Compounds. *Carbon* **2003**, *41*, 1917–1923.

(45) Tan, X.; Fan, Q.; Wang, X.; Grambow, B. Eu(III) Sorption to TiO_2 (Anatase and Rutile): Batch, XPS, and EXAFS Studies. *Environ. Sci. Technol.* **2009**, *43*, 3115–3121.

(46) Yarbaş, T.; Ayas, N. A Detailed Thermodynamic Analysis of CO_2 Hydrogenation to Produce Methane at Low Pressure. *Int. J. Hydrogen Energy* **2024**, *49*, 1134–1144.

(47) Moghaddam, S. V.; Rezaei, M.; Meshkani, F.; Daroughegi, R. Synthesis of Nanocrystalline Mesoporous Ni/$Al_2O_3SiO_2$ Catalysts for CO_2 Methanation Reaction. *Int. J. Hydrogen Energy* **2018**, *43*, 19038–19046.

(48) Deng, L.; Tan, Y.; Chen, C.; Li, F.; Zhang, X. NiCo Composite Catalysts for CO_2 Methanation: The Effect of Preparation Methods on Catalyst Structure and Activity. *New J. Chem.* **2023**, *47*, 8032–8041.

(49) Barreau, M.; Salusso, D.; Li, J.; Zhang, J.; Borfecchia, E.; Sobczak, K.; Braglia, L.; Gallet, J.-J.; Torelli, P.; Guo, H.; Lin, S.; Zafeiratos, S. Ionic Nickel Embedded in Ceria with High Specific CO_2 Methanation Activity. *Angew. Chem. Int. Ed.* **2023**, *62*, e202302087.

(50) Liu, Q.; Bian, B.; Fan, J.; Yang, J. Cobalt Doped Ni Based Ordered Mesoporous Catalysts for CO_2 Methanation with Enhanced Catalytic Performance. *Int. J. Hydrogen Energy* **2018**, *43*, 4893–4901.

(51) Thajudheen, T.; Dixon, A. G.; Gardonio, S.; Arčon, I.; Valant, M. Oxygen Vacancy-Related Cathodoluminescence Quenching and Polarons in CeO_2. *J. Phys. Chem. C* **2020**, *124*, 19929–19936.

(52) Mselmi, F.; Neffati, A.; Kammoun, S. Theoretical Investigation of the Cathodoluminescence Spectra of Co-Doped ZnO Nanowires. *J. Lumin.* **2018**, *198*, 124–131.

(53) Davidson, A.; Tempere, J. F.; Che, M.; Roulet, H.; Dufour, G. Spectroscopic Studies of Nickel(II) and Nickel(III) Species Generated upon Thermal Treatments of Nickel/Ceria-Supported Materials. *J. Phys. Chem.* **1996**, *100*, 4919–4929.

(54) López-Rodríguez, S.; Davó-Quiñonero, A.; Bailón-García, E.; Lozano-Castelló, D.; Villar-Garcia, I. J.; Dieste, V. P.; Calvo, J. A. O.; Velasco, J. R. G.; Bueno-López, A. Monitoring by in Situ NAP-XPS of Active Sites for CO_2 Methanation on a Ni/CeO_2 Catalyst. *J. CO_2 Util.* **2022**, *60*, 101980.

(55) Tang, C.; Li, J.; Yao, X.; Sun, J.; Cao, Y.; Zhang, L.; Gao, F.; Deng, Y.; Dong, L. Mesoporous NiO–CeO_2 Catalysts for CO Oxidation: Nickel Content Effect and Mechanism Aspect. *Appl. Catal., A* **2015**, *494*, 77–86.

(56) Roy, B.; Leclerc, C. A. Study of Preparation Method and Oxidization/Reduction Effect on the Performance of Nickel-Cerium Oxide Catalysts for Aqueous-Phase Reforming of Ethanol. *J. Power Sources* **2015**, *299*, 114–124.

(57) Mao, Z.; Lustemberg, P. G.; Rumptz, J. R.; Ganduglia-Pirovano, M. V.; Campbell, C. T. Ni Nanoparticles on CeO_2(111): Energetics, Electron Transfer, and Structure by Ni

Adsorption Calorimetry, Spectroscopies, and Density Functional Theory. *ACS Catal.* **2020**, *10*, 5101–5114.

(58) Lukashuk, L.; Yigit, N.; Rameshan, R.; Kolar, E.; Teschner, D.; Hävecker, M.; Knop-Gericke, A.; Schlögl, R.; Föttinger, K.; Rupprechter, G. Operando Insights into CO Oxidation on Cobalt Oxide Catalysts by NAP-XPS, FTIR, and XRD. *ACS Catal.* **2018**, *8*, 8630–8641.

(59) Sarnecki, A.; Adamski, P.; Albrecht, A.; Komorowska, A.; Nadziejko, M.; Moszyński, D. XPS Study of Cobalt-Ceria Catalysts for Ammonia Synthesis – The Reduction Process. *Vacuum* **2018**, *155*, 434–438.

(60) Chastain, J.; King, Jr., R. C. *Handbook of X-Ray Photoelectron Spectroscopy*; Perkin-Elmer Corporation, 1992.

(61) Zhou, G.; Liu, H.; Cui, K.; Jia, A.; Hu, G.; Jiao, Z.; Liu, Y.; Zhang, X. Role of Surface Ni and Ce Species of Ni/CeO_2 Catalyst in CO_2 Methanation. *Appl. Surf. Sci.* **2016**, *383*, 248–252.

(62) O'Connor, N. J.; Jonayat, A. S. M.; Janik, M. J.; Senftle, T. P. Interaction Trends between Single Metal Atoms and Oxide Supports Identified with Density Functional Theory and Statistical Learning. *Nat. Catal.* **2018**, *1*, 531–539.

(63) Farmer, J. A.; Campbell, C. T. Ceria Maintains Smaller Metal Catalyst Particles by Strong Metal-Support Bonding. *Science* **2010**, *329*, 933–936.

(64) Zhang, Y.; Zhu, W.; Lu, J.; Liao, W.; Qi, N.; Luo, Y.; Dionysiou, D. D. Induced Synthesis of CeO_2 with Abundant Crystal Boundary for Promoting Catalytic Oxidation of Gaseous Styrene. *Appl. Catal. B* **2024**, *342*, 123461.

TOC Image

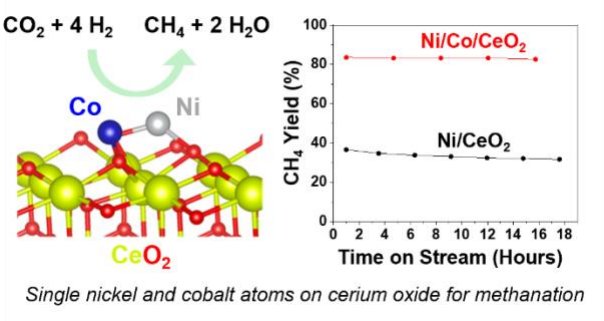

Single nickel and cobalt atoms on cerium oxide for methanation

(65) Kim, H.-M.; Jeong, C. H.; Cheon, B.-S.; Negi, S. S.; Won, W.; Jeong, D.-W. Improving the Performance of a Co-CeO_2 Catalyst for Hydrogen Production via Water Gas Shift Reaction by Addition of Transition Metal Oxides. *Energy Fuels* **2024**, *38*, 4743–4751.

(66) Li, Y.; Zhang, B.; Tang, X.; Xu, Y.; Shen, W. Hydrogen Production from Methane Decomposition over Ni/CeO_2 Catalysts. *Catal. Commun.* **2006**, *7*, 380–386.

(67) Pan, Y.-X.; Liu, C.-J.; Cui, L. Temperature-Programmed Studies of Coke Resistant Ni Catalyst for Carbon Dioxide Reforming of Methane. *Catal. Lett.* **2008**, *123*, 96–101.

(68) Aldana, P. A. U.; Ocampo, F.; Kobl, K.; Louis, B.; Thibault-Starzyk, F.; Daturi, M.; Bazin, P.; Thomas, S.; Roger, A. C. Catalytic CO_2 Valorization into CH_4 on Ni-Based Ceria-Zirconia. Reaction Mechanism by Operando IR Spectroscopy. *Catal. Today* **2013**, *215*, 201–207.

(69) González-Rangulan, V. V.; Reyero, I.; Bimbela, F.; Romero-Sarria, F.; Daturi, M.; Gandía, L. M. CO_2 Methanation over Nickel Catalysts: Support Effects Investigated through Specific Activity and Operando IR Spectroscopy Measurements. *Catalysts* **2023**, *13*, 448.

(70) Le, A. T.; Kim, M. S.; Lee, S. H.; Kim, T. W.; Park, E. D. CO and CO_2 Methanation Over Supported Ni Catalysts. *Catal. Today* **2017**, *293-294*, 89-96.